Nano Research 2018, 11(3): 1389–1398
https://doi.org/10.1007/s12274-017-1754-5
Research Article

ISSN 1998-0124
CN 11-5974/O4

Graphene as an intermediary for enhancing the electron transfer rate: A free-standing Ni_3S_2@graphene@Co_9S_8 electrocatalytic electrode for oxygen evolution reaction

Qiuchun Dong, Yizhou Zhang, Ziyang Dai, Peng Wang, Min Zhao, Jinjun Shao (✉), Wei Huang (✉), and Xiaochen Dong (✉)

Key Laboratory of Flexible Electronics (KLOFE) & Institute of Advanced Materials (IAM), Jiangsu National Synergetic Innovation Center for Advanced Materials (SICAM), Nanjing Tech University (NanjingTech), 30 South Puzhu Road, Nanjing 211816, China

Received: 8 May 2017
Revised: 28 June 2017
Accepted: 30 June 2017

KEYWORDS

three-dimensional,
graphene,
Ni_3S_2@G@Co_9S_8,
oxygen evolution reaction

ABSTRACT

A highly active and stable oxygen evolution reaction (OER) electrocatalyst is critical for hydrogen production from water splitting. Herein, three-dimensional Ni_3S_2@graphene@Co_9S_8 (Ni_3S_2@G@Co_9S_8), a sandwich- structured OER electrocatalyst, was grown *in situ* on nickel foam; it afforded an enhanced catalytic performance when highly conductive graphene is introduced as an intermediary for enhancing the electron transfer rate and stability. Serving as a free-standing electrocatalytic electrode, Ni_3S_2@G@Co_9S_8 presents excellent electrocatalytic activities for OER: A low onset overpotential (2 mA·cm^{-2} at 174 mV), large anode current density (10 mA·cm^{-2} at an overpotential of 210 mV), low Tafel slope (66 mV·dec^{-1}), and predominant durability of over 96 h (releasing a current density of ~ 14 mA·cm^{-2} with a low and constant overpotential of 215 mV) in a 1 M KOH solution. This work provides a promising, cost-efficient electrocatalyst and sheds new light on improving the electrochemical performance of composites through enhancing the electron transfer rate and stability by introducing graphene as an intermediary.

1 Introduction

Traditional energy consumption approaches have caused serious problems, including climate change, extreme weather, haze, and diseases. Therefore, researchers have focused on searching for cleaner energy sources [1–6]. Hydrogen, with a higher calorific value and no emissions, is considered as a green energy source and is one of the most promising clean-energy candidates [7–9]. Among the methods for hydrogen generation, water splitting by electrocatalysts is regarded as the most promising approach because it

---

Address correspondence to Jinjun Shao, iamjjshao@njtech.edu.cn; Wei Huang, iamwhuang@njtech.edu.cn; Xiaochen Dong, iamxcdong@njtech.edu.cn

does not produce pollutants and greenhouse gases [10–12]. Precious metal catalysts have proven highly effective for water splitting, but their applications are tremendously limited by their high cost, scarcity, and poor durability [13–15]. Recently, tremendous efforts are being to develop more economical catalysts, and great progress has been achieved, especially for the hydrogen evolution reaction (HER) [16–21]. However, the oxygen evolution reaction (OER), the other important process of water splitting by electrocatalysts, is still the bottleneck of the entire water electrolysis process because of its sluggish kinetics [22–30].

A three-dimensional (3D) catalytic electrode is a novel structure for high-performance electrocatalysts; it can be prepared by directly depositing catalysts onto a 3D structured substrate or self-assembling the materials into a 3D structure. The 3D structure can effectively reduce the overpotential that results from the binder and contact resistance, which is inevitable in the process where an active powder catalyst is formed in the electrode [31, 32]. Additionally, the 3D catalytic electrode has attracted increasing attention and extensive research efforts [33–38]. For example, Shanmugam et al. directly synthesized an $NiCo_2S_4$ nanowire on nickel foam as a 3D bifunctional electrocatalyst; it presented excellent activity and stability for overall water spitting [39]. Fan et al. built hierarchical porous NiMoN on free-standing carbon cloth as a 3D electrocatalyst for HER [37]. Our previous work also demonstrated that a 3D catalytic electrode based on different 3D substrates can exhibit excellent performances for water splitting [40–42]. However, it is still challenging to design and synthesize an excellent 3D nanostructured material to further and effectively reduce the overpotential of OER.

Herein, we constructed a 3D structured free-standing Ni_3S_2@graphene@Co_9S_8 (Ni_3S_2@G@Co_9S_8) electrode on Ni foam *in situ* using a two-step hydrothermal process. The highly conductive graphene acts as an intermediary layer that can greatly enhance the electron transfer rate between the sulfides. Moreover, the introduction of the graphene layer can improve the durability of the composites by serving as the protecting layer to ensure a uniform coating of Co_9S_8 on Ni_3S_2. Lastly, Ni_3S_2@G@Co_9S_8 was grown on conductive Ni foams *in situ*, providing an excellent stability and conductivity. Due to the synergetic effects from the above-mentioned individual constituents and the complex structure, the resulting Ni_3S_2@G@Co_9S_8 electrocatalyst presented outstanding electrocatalytic activities with a low onset overpotential (2 $mA\cdot cm^{-2}$ at 174 mV), large anode current density (10 $mA\cdot cm^{-2}$ at an overpotential of 210 mV), low Tafel slope (66 $mV\cdot dec^{-1}$), and predominant durability of over 96 h in a 1 M KOH solution.

2 Experimental

2.1 Synthesis of Ni@G

3D Ni@G was prepared by chemical vapor deposition (CVD) under atmospheric pressure, where nickel foam was used as the substrate and ethanol was used as the carbon source (slightly modified from our previously reportedmethod) [43]. Firstly, three pieces of nickel foam (2 cm × 3 cm) were placed in the middle of a quartz tube for 10 min with an argon gas flow to completely discharge air. Secondly, the nickel foam was heated to 900 °C at a fast heating rate under a mixed gas flow (Ar: 40 sccm, H_2: 20 sccm) and maintained for 15 min to clean the nickel foam. Thirdly, ethanol vapor (≥ 99.7%, analytical reagent grade (AR)) was introduced into the pipe by bubbling ethanol liquid with hydrogen and maintained for 20 min. Finally, 3D Ni@G was obtained after rapid cooling to room temperature under argon.

2.2 Synthesis of the 3D Ni@G@Co_3O_4 precursor and Ni@Co_3O_4 precursor

The Ni@G@Co_3O_4 precursor was prepared by a simple solvothermal method, as we previously reported [44], except the nickel foam was replaced by 3D Ni@G. A mixed solution was first prepared by adding ammonia (25%–28% solution in water, AR), sodium carbonate (0.1 M, ≥ 99.8%, AR), and cobalt nitrate (0.1 M, ≥ 99%, AR) in ethylene glycol (≥ 99%, AR) with a volume ratio of 12:50:35:20 under magnetic stirring. The homogeneous solution (15 mL) was transferred into an autoclave with a capacity of 50 mL, and 3D Ni@G was submerged at the bottom of solution; then, the autoclave was placed in an oven for 12 h at 180 °C. 3D Ni@G with the Co_3O_4 precursor was obtained after adequately rinsing with water and vacuum drying overnight. The 3D Ni@Co_3O_4 precursor was obtained using the same procedure, except a piece of clean Ni foam was used instead of 3D Ni@G.

2.3 Synthesis of3D Ni_3S_2@G@Co_9S_8, Ni_3S_2@Co_9S_8, and Ni_3S_2@G

Ni_3S_2@G@Co_9S_8, Ni_3S_2@Co_9S_8, and Ni_3S_2@G were prepared by a simple solvothermal method. A Na_2S (30 mL, ≥ 98%, AR) solution (containing 75 mg of Na_2S) was first prepared in a 50-mL autoclave, and one piece of the 3D Ni@G@Co_3O_4 precursor was submerged in the solution; then, the autoclave was placed in an oven for 24 h at 180 °C. Ni_3S_2@G@Co_9S_8 was obtained after adequately rinsing with water and vacuum drying overnight. Ni_3S_2@Co_9S_8 and Ni_3S_2@G were obtained following the same procedure, except the Ni@Co_3O_4 and Ni@G precursors, respectively, were used instead of Ni@G@Co_3O_4.

2.4 Characterization

The composition and phase of the materials were characterized by X-ray diffraction (XRD; Bruker D8 Advance, Cu Kα energy source) operating at 40 kV and 40 mA. Scanning electron microscopy (SEM; Hitachi, S-4800) and transmission electron microscopy (TEM; JEOL JEM-2010) were used to analyze the morphology and nanostructure of the materials. Raman spectra of the materials were collected using a laser confocal Raman spectrometer (Renishaw in ViaReflex, wavelength: 633 nm). The surface elements and chemical valence state were analyzed by X-ray photoelectron spectroscopy (XPS; PHI 5000 Versa Probe, UIVAC-PHI) with Al Kα radiation.

2.5 Electrochemical measurements

The OER performances of the materials were examined on a Zennium 40667 (ZAHNER) electrochemical workstation operating with a standard three-electrode system in a 1.0 M KOH solution. Typically, a saturated Ag/AgCl electrode (CHI111) was used as the reference electrode, a platinum wire was used as the counter electrode, and the 3D electrocatalyst was directly used as the working electrode without any binder. All the obtained data and relative electrode potentials were calculated to the standard of a reversible hydrogen electrode (RHE) with reference to our previous work (Fig. S1 in the Electronic Supplementary Material (ESM), $E(\text{RHE}) = E(\text{Ag/AgCl}) + 0.925$ V) and without internal resistance (iR) compensation [40].

3 Results and discussion

3.1 Synthesis and structural characterization of materials

Scheme 1 shows the synthetic process for the 3D free-standing Ni_3S_2@G@Co_9S_8 catalytic electrode on the nickel foam template. Firstly, high-quality 3D graphene was synthesized on the surface of the nickel foam using a CVD process [43]. Secondly, the Co_3O_4 precursor was deposited onto the surface of 3D graphene (the Ni@G@Co_3O_4 precursor) using a hydrothermal approach. Finally, the free-standing Ni_3S_2@G@Co_9S_8 electrocatalyst was obtained by sulfuration of the Ni@G@Co_3O_4 precursor using a second hydrothermal process. Ni_3S_2 formed beneath the graphene layer in the sulfuration process; thus, a high-quality graphene layer with unique electrical properties was successfully sandwiched between the catalytically active layers of Ni_3S_2 and Co_9S_8 to enhance the electron transfer rate of the composite electrode.

SEM was employed to study the morphology of the Ni_3S_2/graphene composite. Figure 1(a) shows that the graphene layer is successfully synthesized on the

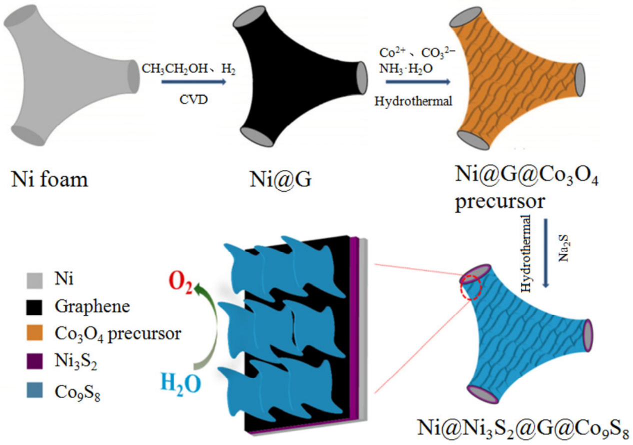

Scheme 1 Schematic illustration of the preparation process for 3D Ni_3S_2@G@Co_9S_8 catalytic electrode.

surface of the nickel foam (Ni@G), which consists of many large graphene islands (diameter ≈ 20 μm). The magnified SEM image in Fig. 1(b) further indicates that the CVD-grown graphene presents a smooth surface and the same topological structure as that for the nickel foam template. After the hydrothermal process with Na_2S, 3D Ni@G is transformed to Ni_3S_2@G. The graphene in Ni_3S_2@G is partly cracked, and Ni_3S_2 nanoparticles are exposed (Fig. 1(c)) because of the volume expansion during the reaction. However, Fig. 1(d) indicates that almost all the large-area graphene sheets are preserved. The XRD pattern of 3D Ni_3S_2@G (Fig. 1(e)) includes a sharp peak (26.8°) attributed to graphene. The other peaks belong to Ni_3S_2 (JCPDS no. PDF#76-1870), except for the three peaks at 44.4°, 51.8°, and 76.3° attributed to Ni (JCPDS no. PDF#87-0712). The Raman spectrum of Ni@G (Fig. 1(f)) exhibits a low peak intensity of the D band (~ 1,336 cm^{-1}), indicating the high quality of the resulting graphene. Moreover, the ratio of the 2D (representing the stacking order of graphene) and G band intensity indicates that 3D graphene consists of one to several layers. Compared with Ni@G, the Raman spectrum of Ni_3S_2@G shows two more peaks at 300.7 and 347.8 cm^{-1} from the formation of Ni_3S_2. The defect peak (D band) and the ratio between the 2D and G band intensities shows essentially no changes with respect to Ni@G, further demonstrating that the high-quality graphene layer of Ni@G is well preserved during the sulfuration process, which is also consistent with the XRD results. These results indicate that the CVD and hydrothermal processes can successfully produce high-quality graphene and the Ni_3S_2/graphene composite, respectively.

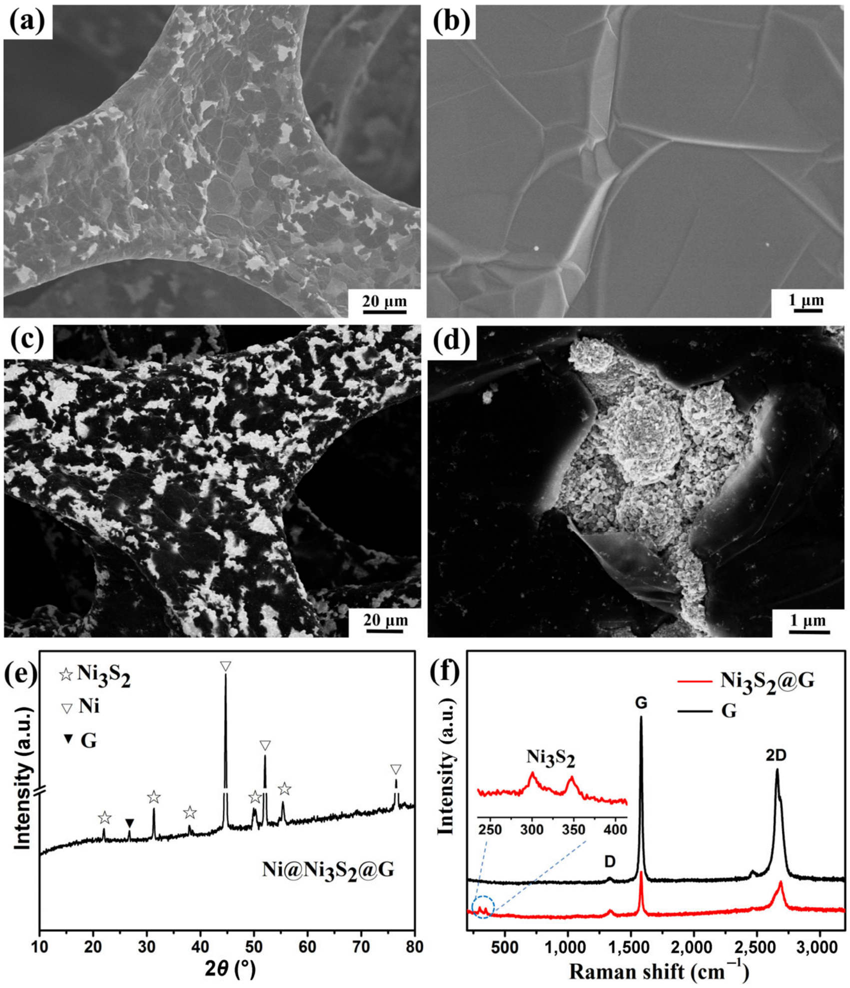

Figure 1 (a) and (b) SEM images of 3D Ni@G, (c) and (d) Ni_3S_2@G at different magnifications. (e) XRD patterns of Ni_3S_2@G, and (f) Raman spectra of Ni@G and Ni_3S_2@G.

XRD and XPS (Fig. 2) were employed to explore the composition of Ni_3S_2@G@Co_9S_8. After sulfuration, the XRD pattern of the Ni@G@Co_3O_4 precursor (Fig. 2(a)) contains more peaks (15.4°, 25.3°, 29.8°, 47.5°, 52.0°) than that of Ni@G (Fig. 1(c)); this difference can be attributed to the planes (111, 220, 311, 511, 440) of Co_9S_8 (JCPDS no. PDF#73-1442). Furthermore, an XRD pattern was collected for the Co_3O_4 precursor after sulfuration under the same conditions (Fig. S2 in the ESM), which matches the standard PDF card of Co_9S_8 (JCPDS no. PDF#73-1442). These results demonstrate that Ni_3S_2@G@Co_9S_8 is successfully synthesized. The elemental distribution and valence state on the surface of Ni_3S_2@G@Co_9S_8 were analyzed by XPS. Figures 2(b)–2(d) show the high-resolution spectrum of Ni 2p, Co 2p, and S 2p, respectively. In the high-resolution spectrum of Ni 2p (Fig. 2(b)), the Ni $2p_{3/2}$ and Ni $2p_{1/2}$ peaks are deconvoluted into five components. The peaks at 854.2, 856.0, and 861.3 eV of Ni $2p_{3/2}$ correspond to Ni (III), Ni (II), and the shake-up peak, respectively. The peaks at 872.8 and 879.4 eV of Ni $2p_{1/2}$ are attributed to Ni (II) and the shake-up peak, respectively [45]. These results are in accordance with a previous report [40]. In Fig. 2(c), the Co 2p region is deconvoluted into four components. The peaks at 780.6 and 785.0 eV of Co $2p_{3/2}$ can be attributed to Co (II) and the shake-up peak. The peaks at 796.4 and 802.6 eV of Co $2p_{1/2}$ correspond to Co (II) and the shake-up peak. In the high-resolution spectrum of S 2p (Fig. 2(d)), the peak is also deconvoluted into four components. The peaks at 161.7 and 162.8 eV correspond to S^{2-}, and the two peaks at 165.1 and 168.5 eV correspond to –C–S– and SO_4^{2-}, respectively [46, 47]; these results agree with the XRD results. The morphologies of the samples were characterized by SEM. Figure S3 in the ESM shows SEM images of the Ni@Co_3O_4 precursor (Figs. S3(a)–S3(c) in the ESM) and Ni_3S_2@Co_9S_8 (Figs. S3(d)–S3(f) in the ESM) at different magnifications. The nanosheets of the Co_3O_4 precursor are compactly and uniformly loaded on the surfaces of the 3D nickel foam in a vertical manner. The morphology of Ni_3S_2@Co_9S_8 obtained by sulfuration of the Ni@Co_3O_4 precursor remains unchanged, and the diameter of the nanosheet is about 5 μm. By comparing the SEM images in Fig. S2 in the ESM and Fig. 3, the morphology of the Ni@G@Co_3O_4 precursor is unchanged after the sulfuration, which was also observed for the Ni@Co_3O_4 precursor; therefore, the introduction of graphene does not change the morphology of the composite. TEM and high-resolution

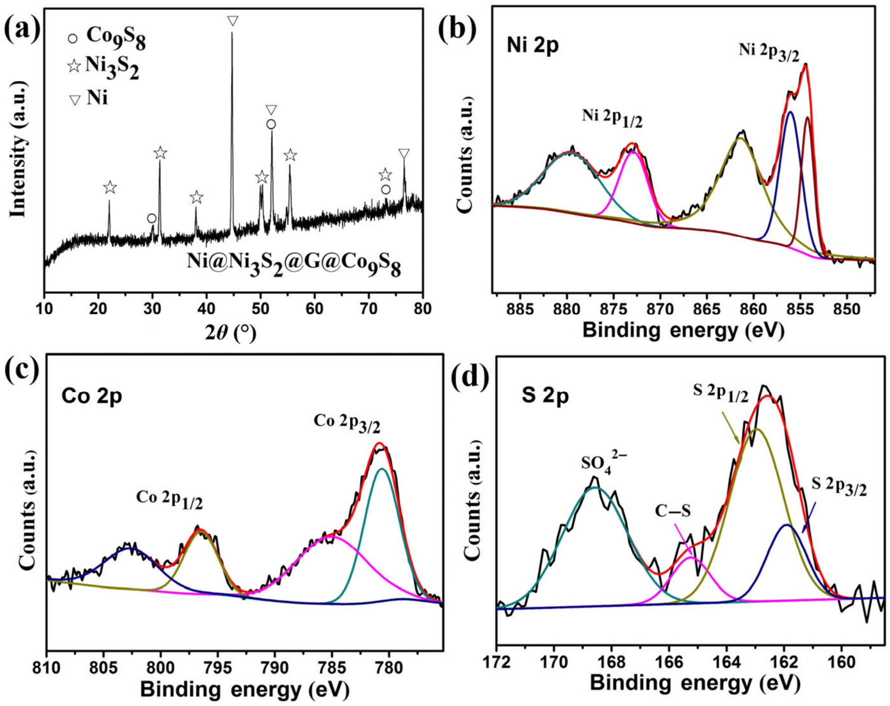

Figure 2 (a) XRD patterns of Ni_3S_2@G@Co_9S_8, (b) Ni 2p XPS spectra, (c) Co 2p XPS spectra, and (d) S 2p XPS spectra.

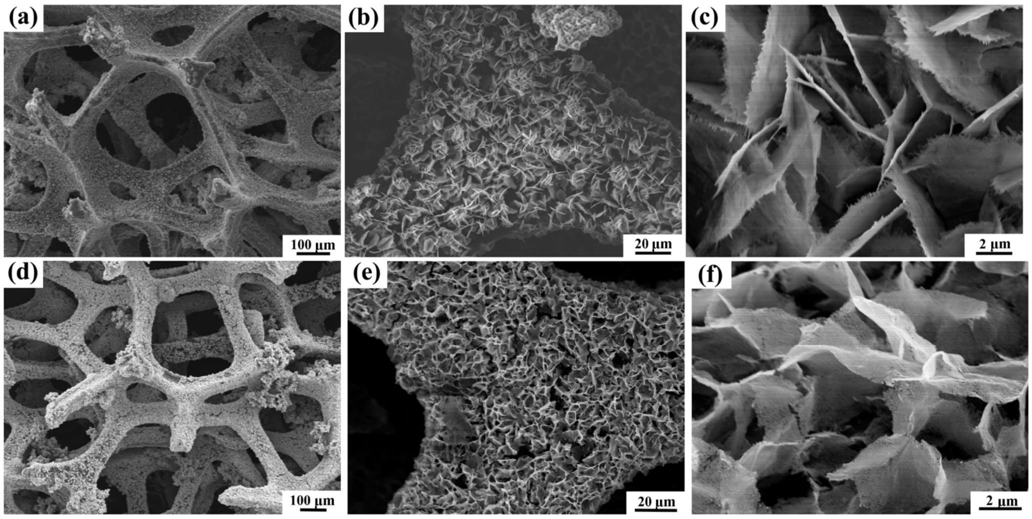

Figure 3 (a)–(c) SEM images of the Ni_3S_2@G@Co_3O_4 precursor at different magnifications. (d)–(f) SEM images of Ni_3S_2@G@Co_9S_8 at different magnifications.

TEM (HRTEM) were further employed to study the structure of Ni_3S_2@G@Co_9S_8. The Co_9S_8 nanosheets show a more porous structure with pore diameters of about 20 nm (TEM image in Fig. 4(a)); these pores can provide more active sites for OER catalysis. The HRTEM image (Fig. 4(b)) shows that the Co_9S_8 nanosheet has an interplanar spacing of 0.57 nm, which corresponds to the (111) plane of the cubic crystal structure of Co_9S_8. The elemental analyses of Ni_3S_2@G@Co_9S_8 (Figs. 4(d)–4(f)) show that Ni, Co, and S are uniformly distributed on the 3D frame. These results demonstrated that the Co_9S_8 nanosheets are successfully loaded onto the surface of Ni_3S_2@G.

3.2 Electrochemical properties

The 3D structured samples are directly used as free-standing electrocatalysts without any binder to evaluate their OER activity. All the test data were collected after the electrocatalysts had reached a stable state by cyclic voltammograms scanning at a rate of 100 mV·s^{-1}. Linear sweep voltammetry (LSV) curves of these 3D electrodes were performed at a rate of 2 mV·s^{-1}. Figure 5 shows the test results for the OER activity. The LSV curves show that the electrocatalytic activity of Ni_3S_2@G@Co_9S_8 is higher than that of Ni_3S_2@Co_9S_8, Ni_3S_2@G, and Ni@G. Additionally, Ni_3S_2@G@Co_9S_8 exhibits a lower onset overpotential (174 mV) than that of Ni_3S_2@Co_9S_8 (183 mV), Ni_3S_2@G (242 mV), and Ni@G (271 mV). To deliver a current density of 10 mA·cm^{-2}, Ni_3S_2@G@Co_9S_8 requires 210 mV, while Ni_3S_2@Co_9S_8, Ni_3S_2@G, and Ni@G need 232, 300, and 345 mV, respectively. Moreover, to deliver 50 mA·cm^{-2}, Ni_3S_2@G@Co_9S_8 requires an overpotential of 283 mV. Figure 5(b) shows the Tafel slopes that correspond to the LSV curves; Ni_3S_2@G@Co_9S_8 presents a smaller slope (66 mV·dec^{-1}) than that of the other electrocatalysts, which illustrates the better chemical dynamics performance for OER. The long-term stability performance of Ni_3S_2@G@Co_9S_8 was tested using chronoamperometry at a constant overpotential of 215 mV. Initially, the current density gradually increases because of the electrocatalyst optimization process; then, it maintains a current density of approximately 14 mA·cm^{-2} for more than 80 h, which shows an excellent stability performance in a 1.0 M KOH solution.

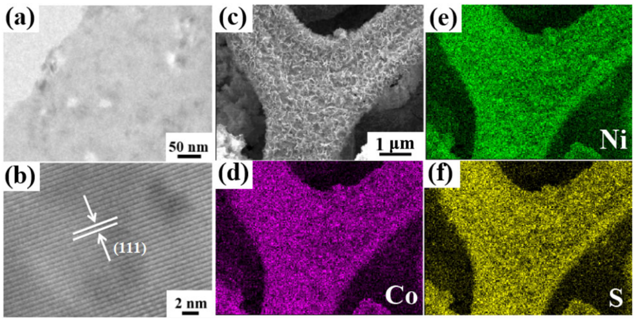

Figure 4 (a) TEM and (b) HRTEM images of Co_9S_8. (c) SEM image and (d)–(f) corresponding elemental analysis images of Ni_3S_2@G@Co_9S_8.

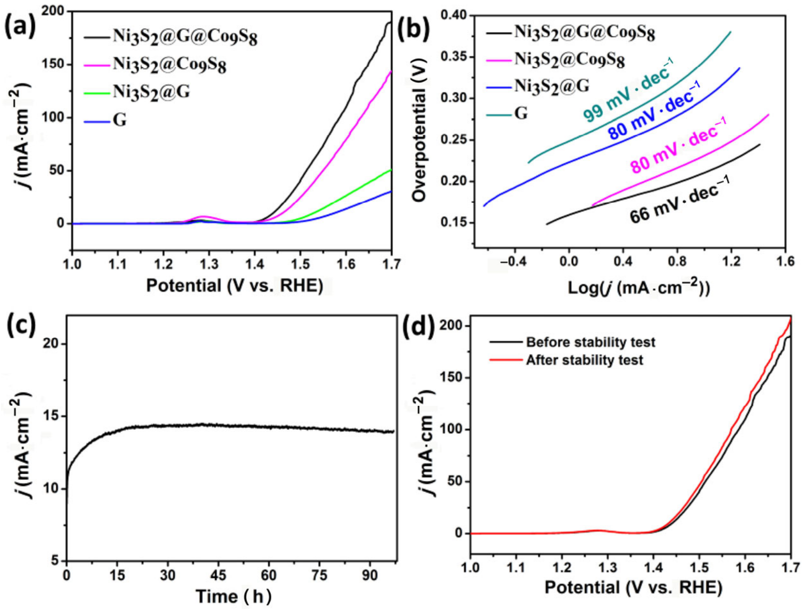

Figure 5 Electrochemical OER activity. (a) LSV curves for Ni@G, Ni_3S_2@G, Ni_3S_2@Co_9S_8, and Ni_3S_2@G@Co_9S_8 measured at 2 mV·s^{-1}, and (b) Tafel slopes of the corresponding LSV curves. (c) Chronoamperometry curve of the Ni_3S_2@G@Co_9S_8 electrode at a constant overpotential of 215 mV. (d) LSV curves of Ni_3S_2@G@Co_9S_8 before and after the chronoamperometry test.

Figure 5(d) shows the LSV curves of Ni_3S_2@G@Co_9S_8 before and after the long-term chronoamperometry measurement, and the catalytic activity of the latter is slightly higher than that of the former, which further demonstrates the superstability performance of Ni_3S_2@G@$Co_9S_8$for OER in a 1.0 M KOH solution. For comparison, Fig. S4 in the ESM shows chronoamperometry measurements and LSV curves of Ni_3S_2@Co_9S_8 before and after the long-term chronoamperometry measurement, and the stability is inferior to that of Ni_3S_2@G@Co_9S_8. The superstability of Ni_3S_2@G@Co_9S_8 can be credited to the introduction of the graphene layer because graphene (as an intermediate layer) provides excellent material compatibility for reducing contact resistance. These results demonstrate that Ni_3S_2@G@Co_9S_8 is an excellent OER catalyst; furthermore, the graphene layer is an effective intermediate layer to improve the catalytic performance because of the increased electron transport rate between the Ni_3S_2 and Co_9S_8 active materials.

Figure S5 in the ESM shows the Nyquist plots of the Ni_3S_2@G@Co_9S_8 and Ni_3S_2@Co_9S_8 electrodes. The Nyquist plots of Ni_3S_2@G@Co_9S_8 show a smaller x-intercept and a larger slope than those of Ni_3S_2@Co_9S_8, which illustrates that the introduction of the graphene intermediary layer can improve the conductivity and enhance the electron transfer rate. The results from the Nyquist plots are in accordance with the electrochemical results.

4 Conclusions

An effective OER catalyst, Ni_3S_2@G@Co_9S_8, was grown *in situ* on Ni foam. An intermediary layer of high quality graphene was sandwiched between the electrochemically active Ni_3S_2 and Co_9S_8 layers. An enhanced electrocatalytic performance was observed because of the improved conductivity and stability endowed by the graphene intermediary layer. Ni_3S_2@G@Co_9S_8 exhibited a higher electrocatalytic performance than that of Ni_3S_2@Co_9S_8 with a low onset overpotential (2 mA·cm^{-2} at 174 mV), large anode current density (10 mA·cm^{-2} at overpotential of 210 mV), low Tafel slope (66 mV·dec^{-1}), and outstanding durability of over 96 h (releasing a current density of ~ 14 mA·cm^{-2} with a constant overpotential of 215 mV) in a 1 M KOH solution. The introduction of graphene is critical for the higher electrocatalytic performance of 3D Ni_3S_2@G@Co_9S_8. This sandwiched structure with graphene as the intermediary sheds new light on the design and construction of new and high-performance electrochemical materials, such as electrocatalysts.

Acknowledgements

The work was supported by the National Natural Science Foundation of China (NSFC) (Nos. 61525402 and 5161101159), Key University Science Research Project of Jiangsu Province (No. 15KJA430006), QingLan Project, National Postdoctoral Program for Innovative Talents (No. BX201600072), China Postdoctoral Science Foundation (No. 2016M601792).

Electronic Supplementary Material: Supplementary material (SEM, XPS and TEM measurements et al.) is available in the online version of this article at https://doi.org/10.1007/s12274-017-1754-5.

References

[1] Roger, I.; Shipman, M. A.; Symes, M. D. Earth-abundant catalysts for electrochemical and photoelectrochemical water splitting. *Nat. Rev. Chem.* **2017**, *1*, 0003.

[2] Ran, J. R.; Zhang, J.; Yu, J. G.; Jaroniec, M.; Qiao, S. Z. Earth-abundant cocatalysts for semiconductor-based photocatalytic water splitting. *Chem. Soc. Rev.* **2014**, *43*, 7787–7812.

[3] Dai, L. M.; Xue, Y. H.; Qu, L. T.; Choi, H. J.; Baek, J. B. Metal-free catalysts for oxygen reduction reaction. *Chem. Rev.* **2015**, *115*, 4823–4892.

[4] Zheng, M. B.; Zhang, S. T.; Chen, S. Q.; Lin, Z. X.; Pang, H.; Yu, Y. Activated graphene with tailored pore structure parameters for long cycle-life lithium-sulfur batteries. *Nano Res.* **2017**, DOI: 10.1007/s12274-017-1659-3.

[5] Zhang, G. X.; Xiao, X.; Li, B.; Gu, P.; Xue, H. G.; Pang, H. Transition metal oxides with one-dimensional/one-dimensional-analogue nanostructures for advanced supercapacitors. *J. Mater. Chem. A* **2017**, *5*, 8155–8186.

[6] Zheng, S. S.; Li, X. R.; Yan, B. Y.; Hu, Q.; Xu, Y. X.; Xiao, X.; Xue, H. G.; Pang, H. Transition-metal (Fe, Co, Ni) based metal-organic frameworks for electrochemical energy storage. *Adv. Energy Mater.* **2017**, DOI: 10.1002/aenm.201602733.

[7] Lewis, N. S.; Nocera, D. G. Powering the planet: Chemical challenges in solar energy utilization. *Proc. Natl. Acad. Sci. USA* **2006**, *103*, 15729–15735.

[8] Bard, A. J.; Fox, M. A. Artificial photosynthesis: Solar splitting of water to hydrogen and oxygen. *Acc. Chem. Res.* **1995**, *28*, 141–145.

[9] Service, R. F. Hydrogen cars: Fad or the future? *Science* **2009**, *324*, 1257–1259.

[10] Turner, J. A. A realizable renewable energy future. *Science* **1999**, *285*, 687–689.

[11] Zou, X. X.; Zhang, Y. Noble metal-free hydrogen evolution catalysts for water splitting. *Chem. Soc. Rev.* **2015**, *44*, 5148–5180.

[12] Tang, C.; Zhang, R.; Lu, W. B.; Wang, Z.; Liu, D. N.; Hao, S.; Du, G.; Asiri, A. M.; Sun, X. P. Energy-saving electrolytic hydrogen generation: Ni_2P nanoarray as a high-performance non-noble-metal electrocatalyst. *Angew. Chem., Int. Ed.* **2017**, *56*, 842–846.

[13] Fournier, J.; Wrona, P. K.; Lasia, A.; Lacasse, R.; Lalancette, J. M.; Menard, H.; Brossard, L. Catalytic influence of commercial Ru, Rh, Pt, and Pd (≦0.1 atomic percent) intercalated in graphite on the hydrogen evolution reaction. *ChemInform* **1992**, *23*, DOI: 10.1002/chin.199246015.

[14] Wang, X. G.; Li, W.; Xiong, D. H.; Petrovykh, D. Y.; Liu, L. F. Bifunctional nickel phosphide nanocatalysts supported on carbon fiber paper for highly efficient and stable overall water splitting. *Adv. Funct. Mater.* **2016**, *26*, 4067–4077.

[15] Lee, Y.; Suntivich, J.; May, K. J.; Perry, E. E.; Shao-Horn, Y. Synthesis and activities of rutile IrO_2 and RuO_2 nanoparticles for oxygen evolution in acid and alkaline solutions. *J. Phys. Chem. Lett.* **2012**, *3*, 399–404.

[16] Zhang, H. C.; Li, Y. J.; Xu, T. H.; Wang, J. B.; Huo, Z. Y.; Wan, P. B.; Sun, X. M. Amorphous Co-doped MoS_2 nanosheet coated metallic CoS_2 nanocubes as an excellent electrocatalyst for hydrogen evolution. *J. Mater. Chem. A* **2015**, *3*, 15020–15023.

[17] Huang, Z. P.; Chen, Z. Z.; Chen, Z. B.; Lv, C. C.; Humphrey, M. G.; Zhang, C. Cobalt phosphide nanorods as an efficient electrocatalyst for the hydrogen evolution reaction. *Nano Energy* **2014**, *9*, 373–382.

[18] Liu, T. T.; Liu, Q.; Asiri, A. M.; Luo, Y. L.; Sun, X. P. An amorphous CoSe film behaves as an active and stable full water-splitting electrocatalyst under strongly alkaline conditions. *Chem. Commun.* **2015**, *51*, 16683–16686.

[19] Wang, S.; Wang, J.; Zhu, M. L.; Bao, X. B.; Xiao, B. Y.; Su, D. F.; Li, H. R.; Wang, Y. Molybdenum-carbide-modified nitrogen-doped carbon vesicle encapsulating nickel nanoparticles: A highly efficient, low-cost catalyst for hydrogen evolution reaction. *J. Am. Chem. Soc.* **2015**, *137*, 15753–15759.

[20] Rowley-Neale, S. J.; Brownson, D. A. C.; Smith, G. C.; Sawtell, D. A. G.; Kelly, P. J.; Banks, C. E. 2D nanosheet molybdenum disulphide (MoS_2) modified electrodes explored towards the hydrogen evolution reaction. *Nanoscale* **2015**, *7*, 18152–18168.

[21] Huang, J. W.; Li, Y. R.; Xia, Y. F.; Zhu, J. T.; Yi, Q. H.; Wang, H.; Xiong, J.; Sun, Y. H.; Zou, G. F. Flexible cobalt phosphide network electrocatalyst for hydrogen evolution at all pH values. *Nano Res*. **2017**, *10*, 1010–1020.

[22] Li, B. B.; Liang, Y. Q.; Yang, X. J.; Cui, Z. D.; Qiao, S. Z.; Zhu, S. L.; Li, Z. Y.; Yin, K. MoO_2-CoO coupled with a macroporous carbon hybrid electrocatalyst for highly efficient oxygen evolution. *Nanoscale* **2015**, *7*, 16704–16714.

[23] Plaisance, C. P.; van Santen, R. A. Structure sensitivity of the oxygen evolution reaction catalyzed by cobalt(II, III) oxide. *J. Am. Chem. Soc*. **2015**, *137*, 14660–14672.

[24] Ma, T. Y.; Dai, S.; Jaroniec, M.; Qiao, S. Z. Metal-organic framework derived hybrid Co_3O_4-carbon porous nanowire arrays as reversible oxygen evolution electrodes. *J. Am. Chem. Soc*. **2014**, *136*, 13925–13931.

[25] Chen, P. Z.; Xu, K.; Fang, Z. W.; Tong, Y.; Wu, J. C.; Lu, X. L.; Peng, X.; Ding, H.; Wu, C. Z.; Xie, Y. Metallic Co_4N porous nanowire arrays activated by surface oxidation as electrocatalysts for the oxygen evolution reaction. *Angew. Chem., Int. Ed*. **2015**, *54*, 14710–14714.

[26] Wang, Y. Y.; Zhang, Y. Q.; Liu, Z. J.; Xie, C.; Feng, S.; Liu, D. D.; Shao, M. F.; Wang, S. Y. Layered double hydroxide nanosheets with multiple vacancies obtained by dry exfoliation as highly efficient oxygen evolution electrocatalysts. *Angew. Chem., Int. Ed*. **2017**, *129*, 5961–5965.

[27] Xu, L.; Jiang, Q. Q.; Xiao, Z. H.; Li, X. Y.; Huo, J.; Wang, S. Y.; Dai, L. M. Plasma-engraved Co_3O_4 nanosheets with oxygen vacancies and high surface area for the oxygen evolution reaction. *Angew. Chem., Int. Ed*. **2016**, *55*, 5277–5281.

[28] Xie, C.; Wang, Y. Y.; Hu, K.; Tao, L.; Huang, X. B.; Huo, J.; Wang, S. Y. *In situ* confined synthesis of molybdenum oxide decorated nickel-iron alloy nanosheets from MoO_4^{2-} intercalated layered double hydroxides for the oxygen evolution reaction. *J. Mater. Chem. A* **2017**, *5*, 87–91.

[29] Liu, Y. Y.; Wang, H. T.; Lin, D. C.; Zhao, J.; Liu, C.; Xie, J.; Cui, Y. A Prussian blue route to nitrogen-doped graphene aerogels as efficient electrocatalysts for oxygen reduction with enhanced active site accessibility. *Nano Res*. **2017**, *10*, 1213–1222.

[30] Zhu, J. Q.; Ren, Z. Y.; Du, S. C.; Xie, Y.; Wu, J.; Meng, H. Y.; Xue, Y. Z.; Fu, H. G. Co-vacancy-rich $Co_{1-x}S$ nanosheets anchored on rGO for high-efficiency oxygen evolution. *Nano Res*. **2017**, *10*, 1819–1831.

[31] Lu, Q.; Hutchings, G. S.; Yu, W. T.; Zhou, Y.; Forest, R. V.; Tao, R. Z.; Rosen, J.; Yonemoto, B. T.; Cao, Z. Y.; Zheng, H. M. et al. Highly porous non-precious bimetallic electrocatalysts for efficient hydrogen evolution. *Nat. Commun*. **2015**, *6*, 6567.

[32] Lu, Z. Y.; Zhu, W.; Yu, X. Y.; Zhang, H. C.; Li, Y. J.; Sun, X. M.; Wang, X. W.; Wang, H.; Wang, J. M.; Luo, J. et al. Ultrahigh hydrogen evolution performance of under-water "superaerophobic" MoS_2 nanostructured electrodes. *Adv. Mater*. **2014**, *26*, 2683–2687.

[33] Huang, J. L.; Hou, D. M.; Zhou, Y. C.; Zhou, W. J.; Li, G. Q.; Tang, Z. H.; Li, L. G.; Chen, S. W. MoS_2 nanosheet-coated CoS_2 nanowire arrays on carbon cloth as three-dimensional electrodes for efficient electrocatalytic hydrogen evolution. *J. Mater. Chem. A* **2015**, *3*, 22886–22891.

[34] Xie, L. S.; Zhang, R.; Cui, L.; Liu, D. N.; Hao, S.; Ma, Y. J.; Du, G.; Asiri, A. M.; Sun, X. P. High-performance electrolytic oxygen evolution in neutral media catalyzed by a cobalt phosphate nanoarray. *Angew. Chem., Int. Ed*. **2017**, *56*, 1064–1068.

[35] Jiang, P.; Liu, Q.; Sun, X. P. NiP_2 nanosheet arrays supported on carbon cloth: An efficient 3D hydrogen evolution cathode in both acidic and alkaline solutions. *Nanoscale* **2014**, *6*, 13440–13445.

[36] Li, S. W.; Wang, Y. C.; Peng, S. J.; Zhang, L. J.; Al-Enizi, A. M.; Zhang, H.; Sun, X. H.; Zheng, G. F. Co-Ni-based nanotubes/nanosheets as efficient water splitting electrocatalysts. *Adv. Energy Mater*. **2016**, *6*, 1501661.

[37] Zhang, Y. Q.; Ouyang, B.; Xu, J.; Chen, S.; Rawat, R. S.; Fan, H. J. 3D porous hierarchical nickel-molybdenum nitrides synthesized by RF plasma as highly active and stable hydrogen-evolution-reaction electrocatalysts. *Adv. Energy Mater*. **2016**, *6*, 1600221.

[38] Xu, R.; Wu, R.; Shi, Y. M.; Zhang, J. F.; Zhang, B. Ni_3Se_2 nanoforest/Ni foam as a hydrophilic, metallic, and self-supported bifunctional electrocatalyst for both H_2 and O_2 generations. *Nano Energy* **2016**, *24*, 103–110.

[39] Sivanantham, A.; Ganesan, P.; Shanmugam, S. Hierarchical $NiCo_2S_4$ nanowire arrays supported on Ni foam: An efficient and durable bifunctional electrocatalyst for oxygen and hydrogen evolution reactions. *Adv. Funct. Mater*. **2016**, *26*, 4661–4672.

[40] Dong, Q. C.; Sun, C. C.; Dai, Z. Y.; Zang, X. X.; Dong, X. C. Free-standing NiO@C nanobelt as an efficient catalyst for water splitting. *ChemCatChem* **2016**, *8*, 3484–3489.

[41] Dong, Q. C.; Wang, Q.; Dai, Z. Y.; Qiu, H. J.; Dong, X. C. MOF-derived Zn-doped $CoSe_2$ as an efficient and stable free-standing catalyst for oxygen evolution reaction. *ACS Appl. Mater. Interfaces* **2016**, *8*, 26902–26907.

[42] Sun, C. C.; Dong, Q. C.; Yang, J.; Dai, Z. Y.; Lin, J. J.; Chen P.; Huang, W.; Dong, X. C. Metal-organic framework derived $CoSe_2$ nanoparticles anchored on carbon fibers as bifunctional electrocatalysts for efficient overall water splitting. *Nano Res*. **2016**, *9*, 2234–2243.

[43] Dong, X. C.; Xu, H.; Wang, X. W.; Huang, Y. X.; Chan-Park, M. B.; Zhang, H.; Wang, L. H.; Huang, W.; Chen, P. 3D graphene-cobalt oxide electrode for high-performance supercapacitor and enzymeless glucose detection. *ACS Nano* **2012**, *6*, 3206–3213.

[44] Meng, S. J.; Wu, M. Y.; Wang, Q.; Dai, Z. Y.; Si, W. L.; Huang, W.; Dong, X. C. Cobalt oxide nanosheets wrapped onto nickel foam for non-enzymatic detection of glucose. *Nanotechnology* **2016**, *27*, 344001.

[45] Zhou, W. J.; Wu, X. J.; Cao, X. H.; Huang, X.; Tan, C. L.; Tian, J.; Liu, H.; Wang, J. Y.; Zhang, H. Ni_3S_2 nanorods/Ni foam composite electrode with low overpotential for electrocatalytic oxygen evolution. *Energy Environ. Sci.* **2013**, *6*, 2921–2924.

[46] Feng, L. L.; Fan, M. H.; Wu, Y. Y.; Liu, Y. P.; Li, G. D.; Chen, H.; Chen, W.; Wang, D. J.; Zou, X. X. Metallic Co_9S_8 nanosheets grown on carbon cloth as efficient binder-free electrocatalysts for the hydrogen evolution reaction in neutral media. *J. Mater. Chem. A* **2016**, *4*, 6860–6867.

[47] Dou, S.; Tao, L.; Huo, J.; Wang, S. Y.; Dai, L. M. Etched and doped Co_9S_8/graphene hybrid for oxygen electrocatalysis. *Energy Environ. Sci.* **2016**, *9*, 1320–1326.